Metal-organic Frameworks derived $Bi_2O_2CO_3$/porous carbon nitride: A nanosized Z-scheme systems with enhanced photocatalytic activity

Ziwei Wang [a,1], Han Wang [a,1], Zhuotong Zeng [b,1], Guangming Zeng [a*], Piao Xu [a*], Rong Xiao [b*], Danlian Huang [a], Xijian Chen [c], Linwei He [c], Chengyun Zhou [a], Yang Yang [a], Zixuan Wang [a], Wenjun Wang [a], Weiping Xiong [a]

[a] *College of Environmental Science and Engineering, Hunan University, Lushan South Road, Yuelu District, Changsha 410082, P. R. China*

[b] *Key Laboratory of Environmental Biology and Pollution Control (Hunan University), Ministry of Education, Lushan South Road, Yuelu District, Changsha 410082, P.R. China*

[c] *State Key Laboratory of Radiation Medicine and Protection, School of Radiation Medicine and Protection, Collaborative Innovation Center of Radiological Medicine of Jiangsu Higher Education Institutions, Soochow University, Suzhou 215123, China.*

* Corresponding author.

Tel.: +86 731 88822754; fax: +86 731 88823701.

E-mail addresses: zgming@hnu.edu.cn (G. Zeng) and piaoxu@hnu.edu.cn (P. Xu) and R. Xiao.

[1]These authors contributed equally to this article.

Abstract

A bismuth-based metal-organic frameworks (MOFs) derived strategy is developed to construct nanoscale $Bi_2O_2CO_3$/porous g-C_3N_4 Z-scheme heterojunction. $Bi_2O_2CO_3$ nanoparticles uniformly distributed in the surface, edge and interlayer of g-C_3N_4 nanosheets, thus significantly increasing intimate contact at the interface. Furthermore, the Z-scheme heterojunctions and doped N atoms escaping from g-C_3N_4 to $Bi_2O_2CO_3$ provided a charge transport chain to promote the charge carriers separation and accelerate the oxidation of $\bullet O_2^-$ by holes, as confirmed by photoluminescence, photoelectrochemical and electron spin resonance measurements. Benefitting from these, the optimized composites not only outperform the pristine g-C_3N_4 in the removal of sulfamethazine (SMT) within 90 min visible light illumination ($\lambda > 420$ nm) but also serve to selectively generate singlet oxygen ($^1O_2$) during the molecular oxygen activation. The present study provides some guidelines for the design of photocatalysts via a MOF-assisted route toward sustainable environmental remediation.

Keywords: Metal-organic frameworks, $Bi_2O_2CO_3$-embedded porous g-C_3N_4, Photocatalytic degradation.

1 Introduction

In recent years, with the growing production of pharmaceutical and personal care products (PPCPs), high-risk antibiotics are ubiquitous in surface water, groundwater and wastewater treatment plants effluents (WWTPs) [1-3]. Among these antibiotics, tetracycline and sulfonamide class are reported as the most famous broad-spectrum antibacterial agent [4, 5]. They are considered to be hazardous for the ecosystem and cause growing concerns to public health, even at low concentrations [6, 7]. Until fairly recently, the roles of WWTPs as resource and route for resistant bacteria releasing to the environment have been acknowledged [8, 9]. Therefore, technologies with high efficiency and sustainable development to reduce antibiotics are urgently needed.

Up to now, great efforts have been dedicated to developing photocatalysts with efficient solar-driven catalytic processes owing to their intriguing prospects for addressing the energy crisis and environmental pollution [10-12]. The latest materials to capture the attention of researchers is graphite carbon nitride (g-C_3N_4), a two-dimensional layer of metal-free polymeric semiconductor [13-15]. The interest in g-C_3N_4 originates from its suitable band gap and excellent physicochemical stability [16, 17]. However, pristine g-C_3N_4 suffers from the poor visible light response, low separation of charge carriers and lack of active sites [18, 19]. Given that photocatalytic performance is closely related to the rational design of photocatalysts, several methods have exhausted to address these drawbacks such as morphology control [20, 21], element doping [22, 23], defect introduction [24] and construction of heterojunction structure [25-28]. Since the pioneering work on Z-scheme systems by Bard et al., the fabrication of Z-scheme heterojunction has received tremendous attention [29]. Commonly, the Z-scheme photocatalysts show satisfactory photocatalytic performance due to its well-matched bandgap structure. Compared with conventional (e.g., type-II)

heterojunction photocatalysts, the Z-scheme structure not only accelerates the spatial separation of charge carriers but also preserves the sufficient energy levels of the photoinduced electrons and holes for the further redox reactions [30, 31].

Bearing these in mind, a series of g-C_3N_4/Bi-based heterostructure photocatalysts have been developed and applied for environmental remediation [8, 32]. Among them, $Bi_2O_2CO_3$ with Aurivillius/Sillén-related structure has been extensively studied. Although the inspiring developments have been obtained, two intractable problems retard the further improvement of high-activity $Bi_2O_2CO_3$/g-C_3N_4 heterojunctions. First, aggregating different materials between interface and hydrothermal strategy are common ways to fabricate heterojunction photocatalysts [32-35]. But these heterojunctions cause the problems of the poor nanoscale contact surface and more inaccessible active sites [36]. Such drawbacks lead to a weak interaction at the contacted surface and a long-distance for electron-hole pairs transfer, resulting in a poor photocatalytic efficiency [37]. Second, the photocatalytic mechanism is deficient. Although the Z-scheme mechanism of $Bi_2O_2CO_3$/g-C_3N_4 has been demonstrated [38, 39], the modulation of interfacial electron flow from charge separation sites to materials surfaces still remains a challenge. Furthermore, both of g-C_3N_4 and bismuth-based semiconductors exhibit great potential for molecular oxygen activation but the synergistic effects between two materials have seldomly been explored [16, 40, 41].

Lately, the pyrolysis of metal-organic frameworks (MOFs), which are a class of emerging crystalline complexes with periodic structures and well-defined nanopores, generates a variety of nanostructured materials with controllable composition and morphology [37, 42-45]. In the past five years, bismuth-based MOFs have received steadily rising interests in the application of smart photonic devices, sensors, and catalysis [46-49]. Among reported four microporous bismuth MOFs, CAU-17, taking

advantage of the excellent stability and economic applicability, has received particular attention [50]. Considering the obvious advantages in controlling the morphology and structure, the rational design of $Bi_2O_2CO_3$/g-C_3N_4 derived from MOF materials is a recommended choice and indeed feasible.

Inspired by these above considerations, we designed a novel composite composed of $Bi_2O_2CO_3$ anchored in porous g-C_3N_4 hybrids via one-shot calcination of the CAU-17/melamine precursor. The metal-organic frameworks acted as a morphology ameliorator, which allowed $Bi_2O_2CO_3$ uniformly to be embedded into porous g-C_3N_4 and simultaneously enlarged the surface area of g-C_3N_4. In this prepared composite, the strong interaction at the interface played significant roles in enhancing visible-light absorption range, and separation of electron-hole pairs. Benefitting from these, the $Bi_2O_2CO_3$/g-C_3N_4 composites exhibit excellent performance in photodegradation results of tetracycline and sulfonamide. Based on trapping experiments and EPR results, we concluded that $Bi_2O_2CO_3$/g-C_3N_4 composites expressly promote molecular oxygen activation into $^1O_2$, which can be ascribed to intimate contact at the interface and construction of Z-scheme system, thereby accelerating the oxidation of $\bullet O_2^-$ by holes. This work provides a promising strategy and in-depth understanding to design highly efficient photocatalysts for environmental remediation.

2 Experimental

2.1 Synthesis

The CAU-17 was prepared under solvothermal conditions according to the previous study [51]. Raw g-C_3N_4 and Bi_2O_3 were prepared by a traditional calcination method [19]. The $Bi_2O_2CO_3$ sample was prepared by a simple solution precipitation method at room temperature. More details are listed in the Supplementary Materials

(SI).

$Bi_2O_2CO_3$/g-C_3N_4 was prepared by a wet chemistry method and calcination. Briefly, a certain amount of CAU-17 was added to 60 mL of water, and the suspension was dispersed by sustaining ultrasonication about 10 min. Then, the 2 g melamine was dissolved in the aqueous dispersion of CAU-17 and stirred for 20 min at 100 ℃. Afterward, the mix solution was gradually cooled down to room temperature to make melamine recrystallization. The mixture was further dried at 100 ℃. Finally, the dried product was calcinated in the ceramic covered crucible and heated at 2.3 ℃ min^{-1} to 550 ℃ and maintained for 4h in air. After cooling to room temperature, the reacted mass was ground to obtain $Bi_2O_2CO_3$/g-C_3N_4 powder. According to the mass ratio of CAU-17 to melamine (1.25%, 2.5%, 5%, 10%), the samples were labeled as BO/CN-1, BO/CN-2, BO/CN-3, BO/CN-4 (BO is $Bi_2O_2CO_3$, CN is g-C_3N_4), respectively.

2.2 Characterization methods

The X-ray diffraction (XRD) measurements were analyzed by BrukerAXS D8 advance with Cu-Kα radiation in the region of 2θ from 5 °to 80 °. The Fourier transform infrared (FT-IR) spectra were recorded on a Bruker spectrometer, scanning from 4000−450 cm^{-1}. The X-ray photoelectron spectroscopy (XPS) measurement was carried out on an Escalab 250Xi spectrometer with Al-Kα X-ray as the excitation source. The ultraviolet-visible (UV–vis) spectra were obtained on a Cary 300 UV−vis spectrophotometer. The BET specific surface area was measured using a Micromeritics ASAP2460. The morphology images of these catalysts were performed using Jeol 2100F transmission electron microscopy (TEM) and JSM-7800F scanning electron

microscopy (SEM). The electron spin resonance (EPR) signals of the radical were collected on Bruker a300. The steady-state and time-resolved fluorescence spectra (PL) were analyzed by Hitachi F7000 fluorescence spectrophotometer. The steady-state, time-resolved fluorescence spectra (PF) and phosphorescence (PH) were analyzed by Hitachi F7000 fluorescence spectrophotometer.

2.3 TMB and NBT measurements

Typically, 40 μL photocatalysts (4 g/L) was added into 2 mL 3,3′,5,5′-tetramethylbenzidine (TMB) solution prior to the test. The solvent was HAc/NaAc buffer solution (pH=3.7) and the concentration of TMB was 50 mM. The light source was a 300W Xe lamp with a 420 nm pass filter. The optical absorption intensity at 380 nm of the oxidation of TMB solution was measured to determine the TMB concentration by using a UV−vis spectrophotometer. To identify reactive oxygen radicals, different amounts of scavengers were put into the suspension liquid before the UV–vis measurements: (I) carotene (4mg); (II) mannitol, 50 mM, 100 μL; (III) catalase, 4000 units/mL, 100 μL; (IV) superoxide dismutase (SOD), 2500 units/mL, 200 μL. Nitroblue tetrazolium (NBT) transformation test was used to measure the concentration of $\bullet O_2^-$. In each experiment, a 50 ml solution containing 0.015 mM NBT and 50 mg photocatalysts for photocatalysis studies. The optical absorption intensity at 260 nm of the obtained NBT solution was measured to determine the NBT concentration by using a UV−vis spectrophotometer.

2.4 Photocatalytic activity.

The light source was a 300W Xe lamp with a 420 nm pass filter. In each experiment,

a 50 ml solution containing a desired amount of SMT (or 60 ml TC) and 50 mg (30 mg for TC) photocatalysts for photocatalysis studies. The mixture solutions were stirred in the dark for 30min in order to ascertain adsorption equilibrium. During the irradiation, about 3.5 mL aliquots were sampled at certain time intervals, followed by filtering with syringe membrane filters (0.22 μm) to remove catalyst particulates. The optical absorption intensity at 357 nm of the obtained TC solution was measured to determine the TC concentration by using a UV−vis spectrophotometer. The residual concentration of SMT was filtered and detected by the high-performance liquid chromatography (HPLC). The total organic carbon (TOC) remaining in the solution of SMT and TC was studied by a TOC analyzer (Analytikjena multi N/C 2100). Furthermore, the degradation intermediates of SMT were detected by HPLC-MS and a detailed analysis method in this study is illustrated in the SI.

3 Results and discussion

3.1 Photocatalysts characterization.

The synthetic process of BO/CN is illustrated in Scheme 1. The CAU-17 was prepared under solvothermal conditions and the XRD pattern of prepared CAU-17 is well consistent with the previously reported (Fig. S1a). SEM (Fig. 1a, and S1c) and TEM (Fig. S1d) images demonstrated that CAU-17 is a hexagonal prism structure, where the prisms have a width of ~2 μm and the lengths of ~20 μm. Subsequently, the obtained CAU-17 was used as a matrix to anchor melamine via a recrystallization process. The formation of BO/CN was primarily ascribed to the pyrolysis process of CAU-17/melamine precursor. Only the diffraction peaks of monoclinic phase Bi_2O_3

(PDF no. 41-1449) was detected in the XRD pattern after the calcination of CAU-17 without the addition of melamine (Fig. S1b) [8]. These changes from Bi-O bonds of Bi_2O_3 to Bi-O-C bonds in $Bi_2O_2CO_3$ may be caused by the strong interfacial coupling effects between CAU-17 and melamine [39]. Carbon dioxide (CO_2) gas released from the pyrolysis of melamine then further promotes the construction of Bi-O-C bonds [32, 52]. The morphology of CAU-17, Bi_2O_3, and g-C_3N_4 are investigated by SEM. The morphology of obtained Bi_2O_3 was completely different from the CAU-17, suggesting the collapse of the structure after the calcination (Fig. 1b). Interestingly, the flocculent rods of obtained Bi_2O_3 suggest the existence of a carbon bridge, which is also proved by the XPS analysis (Table S1). For the pristine g-C_3N_4, a typical plate-like structure can be seen (Fig. 1c). The local structure is further imaged by TEM (Fig. 2a), which possesses a porous structure.

After $Bi_2O_2CO_3$ loading, a clear change in the morphology of BO/CN was observed, as manifested by the appearance of a frizzy porous structure in $Bi_2O_2CO_3$/g-C_3N_4 (Fig. 1 d-e). This change may endow the composite with a larger surface area and more active sites. This conclusion is also proved by the desorption isotherm and pore volume (Fig. S2). Although the BET surface areas decreased from 40.72 m^2g^{-1} to 26.01 m^2g^{-1} when the CAU-17 mass ratio was further increased from 5% to 10%, all the composites exhibited higher BET surface areas than pristine CN. This property would favor the contact between heterojunction and antibiotics, thereby improving the photocatalytic degradation performance [53]. As shown in Fig. 1, the SEM-EDS element mapping of BO/CN further confirmed the existence of Bi, C, O, N elements

that are uniformly distributed. TEM image is carried out to directly observe the dispersion of $Bi_2O_2CO_3$ on g-C_3N_4. These images indicated that $Bi_2O_2CO_3$ is uniformly anchored into porous g-C_3N_4. The high-resolution TEM image (HRTEM) clearly revealed that the lattice spacing of 0.2735 nm corresponding to the (110) lattice planes of $Bi_2O_2CO_3$ (Fig. 2c, d). Fig. 2 f-i shows the HAADF-STEM images in $Bi_2O_2CO_3$/g-C_3N_4 heterojunction. As expected, the N element was also detected on the surface of $Bi_2O_2CO_3$ nanomaterials, which convincingly prove the close incorporation between two phases [39].

Fig. 3a illustrates the XRD pattern of BO/CN. The peaks at 27.3° and 13° could be assigned to the (100) and (002) facets of pristine g-C_3N_4 [27]. After $Bi_2O_2CO_3$ loading, the additional characteristic peaks at 23.98°, 30.2°, 32.8°, and 56.9° appeared in all samples of $Bi_2O_2CO_3$/g-C_3N_4, which are corresponded to (011), (013), (110) and (123) of the tetragonal phase $Bi_2O_2CO_3$ (PDF no. 41-1488). Furthermore, the peaks of g-C_3N_4 became weaker and regularly, toward higher angles with the increase of CAU-17, indicating that the distuibance of the packing of the singlet layers and increased content of uncrystallized g-C_3N_4 [54]. For BO/CN-4, the peaks of Bi_2O_3 at 28.1° are found which indicates that the transformation from Bi-O bonds to Bi-O-C bonds is not complete [52]. Furthermore, the enhanced characteristic peak of $Bi_2O_2CO_3$ in the XRD pattern suggested the larger particles and more ratio of $Bi_2O_2CO_3$ in the heterojunction. It may result in an agglomeration effect and thus destructing the crystal structure of g-C_3N_4 by squeezing g-C_3N_4 nanosheets [39].

The FTIR spectroscopy of pristine g-C_3N_4 and BO/CN in Fig. 3b presents similar

symmetric and asymmetric stretching, suggesting the maintenance of a similar framework in the composites. The typical variation band located at 1200-1700 cm^{-1} are corresponding to vibrations of CN heterocycles, and the peaks located at 808 cm^{-1} are due to the typical out-of-plane bending vibration of tri-s-triazine-based structure [55]. Compared to g-C_3N_4, the 808 cm^{-1} peaks of $Bi_2O_2CO_3$/g-C_3N_4 slightly red-shifted to high frequencies which indicated the weakened interaction between "nitrogen pots" in $Bi_2O_2CO_3$/g-C_3N_4 [56]. Besides, the slightly enhanced intensity of a new peak at 2165 cm^{-1} suggested that CAU-17 addition during the pyrolysis process introduced -C≡N groups (Fig. 3c) [24]. These changes are likely due to the partial N of g- C_3N_4 doping into $Bi_2O_2CO_3$ to construct trace amount Bi-N bonds. Commonly, these changes would alter the corresponding electronic structure and construct the unpaired electrons [43]. As one of the most efficient techniques for measuring the spin state of unpaired electrons, EPR spectra were employed to provide more direct evidence. As shown in Fig. 3d, the BO/CN exhibited remarkably enhanced EPR signal at the around g value (2.003) in comparison with g-C_3N_4, owing to the increased unpaired electrons by the formation of Bi-N bonds [39]. The slightly EPR signal was detected for the g-C_3N_4, which may be due to the inherent defect sites.

The detail surface elemental composition and chemical states of g-C_3N_4 and BO/CN are further investigated via XPS analysis. As shown in Fig. S3, the survey scanning spectrum verified that BO/CN was mainly composed of Bi, C, O, N elements, which are corresponding well to the peaks at around 159 eV, 288 eV, 398 eV, and 531 eV. N/C atom ratios for g-C_3N_4 and BO/CN were also listed in Table S2. Noted that a

slight decrease of N/C atom ratios is observed in the XPS spectra of BO/CN, which further proves the construction of heterojunction. Fig. 4a shows C 1s spectrum, the peaks divided into 288.9 eV, 288 eV, 286.4 eV, and 284.6 eV can be assigned to C-O band (C1), sp^2 -hybridized carbon (N=C−N, C2), CH-N on the edges of heptazine unit (C3) and C−C/C=C (C4) [14, 57]. Compared to g-C_3N_4, two alternations in the C 1s spectrum of BO/CN could be observed. The first alternation is the decreased value of C2: C4 from 7.07 to 5.14 (Table S3), which originated from the additional C=C bond and carbonate ion of $Bi_2O_2CO_3$ [58]. Then, the increased area ratios of C3 may be due to the enhancement of surface and edge [24]. The high-resolution N 1s spectrum of g-C_3N_4 and BO/CN (Fig. 4b) can be divided into three peaks at 400.1 eV, 399.8 eV and 398.2 eV, which could be ascribed to the terminal C–N-H amino functions (N1), the inner atoms bonded with the N-$(C)_3$ groups of skeleton (N2) and the sp^2-bonded nitrogen in s-triazine ring (C=N-C, N3) [59]. After loading with $Bi_2O_2CO_3$, the slight positive shift of N2 and N3 in the heterojunction indicates that $Bi_2O_2CO_3$ interacts with sp^2-bonded nitrogen and bridging nitrogen, which constructs a new Bi-N bond and the distribution of the electric charge. This is further confirmed by the Bi 4f and O 1s spectrum. For BO/CN, the band energies of Bi 4f 7/2 and 4f 5/2 peaks shift from 159.69 eV and 164.98 eV to 159.1 eV and 164.3 eV, respectively (Fig. 4d). Fig. 4d exhibits the O 1s spectrum of Bi_2O_3, BO/CN-3, and CN. The peaks at 533.5 eV and 531.65 eV could be ascribed to O_2 and H_2O, which maintain unchanged. Conversely, the peak at 530.3 eV corresponding to O atoms in the Bi-O layers of Bi_2O_3 was shifted to 529.5 eV in BO/CN-3. This phenomenon that N atoms on the heterojunction possess higher binding

energy compared to pristine g-C_3N_4 may be ascribed to the escape of electrons in the conjugated system, resulting in the decrease of electron density [43]. Reversely, the Bi and O atoms obtaining electrons would increase electron density and possessed lower binding energy. Therefore, these results prove that Bi-N bonds could be formed at the interface, thus altering the charge distribution and resulting in the enclosed shifts of binding energy [58].

3.2 Optical property

These unique structural features of BO/CN such as frizzy porous, intimate contact and strong interaction at the interface are supposed to significantly impact the optical excitation processes. UV−vis diffuse absorption spectrum is used to investigate the visible light absorption range of g-C_3N_4 and BO/CN, which determines the number of incident photons joining into photocatalytic reaction. As shown in Fig. 5a, with the increasing CAU-17 usage from 1.25% to 5%, the absorption edge showed a remarkable redshift along with a broader absorption tail. This characteristic is also reflected in the physical crystal appearance: the brown color increase in intensity. The bandgaps of CN and BO are evaluated to be 2.56 eV and 3.2 eV based on the transformed Kubelka–Munk function, which is in agreement with the previous report [19, 27]. (Fig. 5b). According to previous studies and DFT calculation [33, 60], the E_{CB} and E_{VB} of BO are estimated to 0.26 eV and 3.46 eV (vs. NHE) based on the Mulliken electronegativity theory (the details of the estimation are provided in the Text 3). As depicted in Fig. S4, the positive slope of Mott-Schottky plots displayed that g-C_3N_4 was an n-type semiconductor. The flat band potential of g-C_3N_4 was estimated to -1.02 eV versus

289 Ag/AgCl electrode, which is corresponding to -0.82 eV versus normal hydrogen
290 electrode. For n-type semiconductor, the Fermi level was approximately equal to the
291 conduction band edge. Thus, the CB edge potential of g-C_3N_4 was -0.82 eV. According
292 to the equation of $E_{CB} = E_{VB} - E_g$, the E_{VB} of CN was determined as 1.74 eV. Therefore,
293 when $Bi_2O_2CO_3$ contacted with g-C_3N_4 each other, a built-in electric field was
294 constructed at the interface.

295 Excitonic effects, originating from the Coulomb interactions between
296 photoinduced holes and electrons, play a significant influence on the photocatalytic
297 process [61]. PF spectra such as steady-state and time-resolved cases are important
298 techniques to explore the photoexcitation process. As shown in steady-state
299 fluorescence spectra (Fig. 6a), CN possessed a strong emission at the wavelength of
300 470 nm owing to the radiative recombination of charge carriers. Compared to CN, the
301 composite BO/CN presented an apparent quenched PF signal, suggesting the
302 remarkably spatial separation of electron-hole pairs. Time-resolved fluorescence
303 spectra were further performed at their corresponding steady-state emission peaks yield
304 to calculate the average radiative lifetime (Fig. 6b). A double-exponential function fits
305 the decay (More details are listed in Text S4), yielding the radiative average lifetime of
306 ≈ 7.24 ns and 4.97 ns for CN and BO/CN-3. This dramatically reduced shorter lifetime
307 could be ascribed to the enhancement of spatial charge separation, which depresses the
308 recombination of electron-hole pairs [62].

309 Furthermore, the nanosized heterojunction that we designed and illustrated here is
310 a novel subject for the $Bi_2O_2CO_3$/g-C_3N_4 family, because it possesses nanometer-scaled

structures and has Bi-N bonds as the linkers between interlayers. Compared with Van der Waals heterostructures, such as BO-CN-Mix [32-35], this kind of chemical bond could provide an electron shuttle pathway to accelerate the interfacial charge flow [58, 63]. To investigate the interfacial electron transfer, the electrostatic potential of BO/CN heterojunction with and without Bi-N bonds was also carried out using theory calculations. As shown in Fig. 6c, d, when the BO and CN interact with Bi-N bonds, the interfacial electron flow need to overcome a 27 eV energy barrier and a 4.1 Å transfer distance. By contrast, the interaction with Van der Waals force increase the energy barrier and transfer distance by 5 eV and 1.4 Å, respectively, indicating the Bi-N bonds energetically promote the electron transfer. To verify this theory calculation, transient photocurrent response curves and EIS are applied to better investigate interfacial charge transfer behaviors. The photocurrent response results (Fig. 6e) indicate that CN, BO/CN are stable in response to each illumination. As expected, these composites show an obvious higher photocurrent response density than CN. The decreased arc radius of Nyquist plots (Fig. 6f) also indicates that interaction between $Bi_2O_2CO_3$ and g-C_3N_4 could effectively reduce the charge transfer resistance at the material interface. Moreover, the slopes of Mott-Schottky plots (Fig. S4) exhibited that BO/CN composites possess higher carrier density, which indicates the ultrafast spatial charge separation efficiency [14]. Hence, the photoinduced electrons and holes are efficiently separated by strong interaction and exciton dissociation. Then, the Bi-N bonds formed at the interface provide a transfer high-pathway for the separated electrons to participate in the further redox reaction.

3.3 Photocatalytic Activities

The photocatalytic performance of CN and BO/CN is estimated by the degradation of antibiotics under visible light irradiation, including TC and SMT (Fig. S5). Fig. 7a shows the photodecomposition efficiency of CN and BO/CN. It can be observed that nearly no SMT decomposition occurs in the absence of photocatalysts. The CN had a certain catalytic activity for the photodegradation of SMT under visible light illumination. The removal efficiency was 38.35% within 90 min. As expected, all the BO/CN composites displayed superior photocatalytic decomposition efficiency compared to CN. Among them, BO/CN-3 exhibited the highest photocatalytic performance (90.31%) for the degradation of SMT in 90 min with an enhancement of 51.96% compared to pristine CN. However, the degradation efficiency of SMT decreased from 90.31% to 78.3% when the mass ratio of CAU-17 increased from 5% to 10%. This indicates that the excessive CAU-17 usage exhibited negative effects on CN photolysis, probably because the agglomeration effect of $Bi_2O_2CO_3$ destroys the crystal structure of g-C_3N_4. The excessive $Bi_2O_2CO_3$ nanoparticles in the heterojunction squeeze g-C_3N_4 nanosheets rather than implant into the interlayers. As a result, the BO/CN-4 possess lower charges separation efficiency and surface area and exhibited inhibited photocatalytic activities [64].

As shown in 7b, we use the pseudo-first-order kinetic model displayed by the linear transformation ln (C_0/C) = kt to analyze photocatalytic reaction kinetics of SMT degradation. In the same circumstance, the BO/CN-3 showed the apparent rate constants about 0.026 min^{-1}, which was 5.2 times higher than that of CN. To accurately

investigate the different photocatalytic activities, the corresponding rate constant k to the specific surface area was also normalized (Table. S4). Obviously, the BO/CN-1 still exhibited ~3.36 times higher activity than that of CN, suggesting the enlarged surface area make a minor devotion to enhancing photocatalytic degradation [58]. It was inferred that the synergistic effects between BO and CN rather than increased surface area reinforce the photocatalytic capacities under visible light. Fig. 7c is the HPLC data of SMT decomposition by BO/CN-3. The distinct SMT adsorption peak can be observed at 2.26 min in the chromatogram. With reaction time going on, this absorption peak remarkably decreased. It has been well established that the initial concentration has an important impact on the efficiency of the degradation of the pollutant during the photocatalytic process [51]. Fig. 7d shows the degradation efficiency of BO/CN-3 with different initial SMT concentrations. The corresponding decomposition rates are 100%, 90.31%, 81.42% and 61.35% when the initial SMT concentration equaled to 5, 10, 15, and 20 mg/L, respectively. Commonly, the higher initial concentration of pollutants suppresses photons entering the photocatalytic reaction and the production of reactive radicals [65-67]. Besides, the intermediates originating from the degradation process could compete with SMT pollutants and take over some surface-active sites, thus further inhibiting the degradation rates.

TG analysis reveals that CAU-17 is thermally robust and there are two weight loss processes between 30 ℃ and 600 ℃ (Fig. S5a). The first process up to 100 ℃ is ascribed to the desorption of free water molecules and solvent methanol molecules. Then, the framework collapses and the BTC linker is lost at 450 ℃ [48]. Therefore,

different calcination temperatures at 450 ℃, 500 ℃, 550 ℃ and 600 ℃ were set to investigate the influence on photocatalytic activities. The corresponding decomposition rates are shown in Fig. S5b. With an increase of temperature from 450 ℃ to 550 ℃, the SMT removal rates significantly increased from 39.94% to 90.31%. Further increasing temperature to 600 ℃, the decomposition efficiency decreased to 80.56%. Generally, calcination conditions can determine phase composition and interaction between the components. For 600 ℃, the decreased characteristic peak of $Bi_2O_2CO_3$ in the XRD pattern suggested less ratio of $Bi_2O_2CO_3$ in the heterojunction. It may result in a weak interaction at the interface and the limited electron transfer, thus inhibiting the degradation of SMT.

To fully investigate the degradation pathway of SMT by the CN and BO/CN, LC-MS analyze is further performed to identify a reasonable degradation pathway. Fig. S6 shows the MS spectra and possible chemical structure of several intermediates that are discovered during the degradation process. As shown in Fig. 8, the intensity of SMT peak (m/z 279) decreased rapidly with the reaction time, suggesting the excellent photo-oxidation capability of BO/CN. Subsequently, two peaks of products appeared between 1.860 min and 2.100 min, and the intensity increased firstly and then decreased along with the increasing of the reaction time. It indicates that these intermediates are oxidized and mineralized to harmless inorganic molecules. In this context, three main detected intermediates of SMT are possibly identified as N-(4, 6-dimethylpyrimidin-2yl) benzene-1, 4-diamine (I, m/z 215), 4, 6-dimethylpyrimidin-2-ol (II, m/z 124) and 4-aminophenol (III, m/z 110). According to these intermediates and similar studies

399 published previously, the possible degradation of SMT is proposed in Fig. 8 [8, 68, 69].
400 Thus, we can speculate that the initial degradation is companied with SO_2 elimination
401 led that product I is 64 atomic mass unit (amu) less than SMT molecule. Then, the
402 product II and III are further formed by the bond cleavage of C-N. Finally, these
403 intermediates were completely degraded into H_2O, CO_2, and NH^{4+}, etc.

404 Apart from SMT, TC is also one of the broad-spectrum antibacterial agents, which
405 can cause the disruption of the microbial population [57]. Fig. 7e shows the
406 photodecomposition rates of TC by CN and BO/CN. After compounding $Bi_2O_2CO_3$
407 with porous g-C_3N_4, the photodecomposition rates were significantly increased. The
408 BO/CN-3 effectively degraded more than 83% of TC within 60 minutes of visible light
409 illumination in comparison with 42% by pristine g-C_3N_4. Moreover, the degradation
410 efficiency of BO/CN is higher than most of $Bi_2O_2CO_3$-based, MOF-derived and g-
411 C_3N_4-based (melamine) photocatalysts reported previously (Table 1), indicating that
412 Bi-based MOF derivates/ porous g-C_3N_4 composites are a promising photocatalytic
413 system for environmental remediation. The complete removal of SMT and TC achieved
414 in the photocatalytic process are crucial to prevent secondary pollution [44]. Therefore,
415 the ability of mineralization also is an important indicator of photocatalysts. Fig. 9a
416 clearly indicates that the mineralization efficiency of SMT reaches 42% within 180 min
417 visible light irritation. As for TC, the prepared composites BO/CN shows a 35%
418 mineralization efficiency of TC within 120 min visible light irritation (Fig. S7a). These
419 results confirm that BO/CN could actually mineralize SMT and TC into intermediate
420 compounds or CO_2 and H_2O.

Commonly, the practical application of photocatalysts largely depends on their stability. For this reason, we conduct recycling photocatalytic experiments to investigate the reusability of BO/CN. After each cycling reaction, BO/CN is collected from aqueous suspension by filtration, washed with ethyl alcohol and deionized water 5 times to absolutely remove the absorbed pollutants. As presented in Fig. 9b and Fig. S7b, the photocatalytic degradation efficiency of TC and SMT slightly reduced by 5% and 6% after four cycles, respectively. In addition, the chemical stability of the BO/CN used, under rough experimental conditions, is examined by XRD, FT-IR and SEM (Fig. S8). The used composites maintained the crystallinity, composition and morphology structure even after four circles, indicating good stability. The stability of BO/CN was also proved by monitoring the leaching of bismuth ions during the reaction process. As displayed in Table S5, the bismuth ions leached from BO/CN was less than 0.0026 mg/L (the leaching rate of BO/CN-3 was 0.025 %), which also suggested excellent stability of BO/CN [70]. Based on the above results, it is demonstrated that BO/CN can perform as a promising photocatalyst for the photocatalytic decomposition of antibiotics.

3.4 Possible degradation mechanism.

To better uncover the reaction mechanism, we conduct species trapping experiments to systematically elucidate the reactive radicals of BO/CN-3 and CN on the decomposition of SMT under visible light illumination. In these two cases, EDTA-2Na, isopropanol (IPA), TEMPOL and sodium azide act as holes, •OH, $•O_2^-$ and $^1O_2$ scavengers, respectively [71]. For BO/CN-3 case shown in Fig. 7f, the photocatalytic

443 removal efficiency of BO/CN-3 was decreased to 21% in the presence of EDTA-2Na,
444 indicating the holes were the main reactive species. Furthermore, $^1O_2$ and $\bullet O_2^-$ were
445 found to perform fewer influences on SMT degradation, whereas •OH was inclined to
446 have a neglectable role. On the other hand, $\bullet O_2^-$ mainly account for antibiotics
447 degradation in the CN case, pointing a different ROS generation pathway between
448 BO/CN-3 and CN.

449 Then, the ROS generation was investigated by using TMB as a probe molecule,
450 which could react with different ROS and show an increase of the absorption intensity
451 at about 380 nm. As shown in Fig. 10a, the absorption increases of TMB solution
452 distinctly suggested the generation of ROS for both g-C_3N_4 and BO/CN-3. Especially,
453 the BO/CN-3 samples show much improved molecular oxygen activation ability. The
454 trapping experiments were further conducted to systematically elucidate the reactive
455 ROS on the oxidation of TMB under visible light illumination. In the two cases,
456 carotene, mannitol, catalase and superoxide dismutase act as $^1O_2$, •OH, H_2O_2 and $\bullet O_2^-$
457 scavengers, respectively. As displayed in Fig. 10b, remarkable suppression of TMB
458 oxidation was found in the presence of carotene, whereas the other scavengers exhibit
459 negligible effects on the oxidation rate. Obviously, we infer that the singlet oxygen $^1O_2$
460 is the main reactive ROS for BO/CN-3. On the contrary, the oxidation ability of CN
461 changed with the addition of mannitol and SOD, showing that •OH and $\bullet O_2^-$ are what
462 accounts for photoinduced ROS. Taken together, it can be summarized the BO/CN
463 composites could generate more $^1O_2$ during the molecular oxygen activation and the
464 holes were found to execute more important influences on antibiotics decomposition

[72].

Based on the above results, the EPR spin-trapping experiments were measured on both CN and BO/CN-3 for identifying reactive radicals. TEMP, TEMPO and DMPO were used as the trapping agent for the detection of $^1O_2$, •OH, $•O_2^-$ and holes, respectively [73]. The related results are displayed in Fig. 10 c-f. It is clear that CN/BO-3 displayed much higher signal intensity of $^1O_2$ and holes while CN tend to generate •OH and $•O_2^-$. The reason for the decrease of $•O_2^-$ could be ascribed to the generation of $^1O_2$. In such a system, the BO/CN significantly boosts the molecular oxygen activation into $^1O_2$, which is benefits from the strong interaction and formation of Bi-N bonds at the interface, thus promoting spatial charge separation and the oxidation of $•O_2^-$ by holes [40, 74]. This further confirmed by the NBT transformation experiments. As illustrated in Fig. S9a, the continuous decrease in absorbance (260 nm) displayed the oxidation of NBT by CN, while the BO/CN-3 exhibited much lower catalytic activity. Based on our previous study [27], the average $•O_2^-$ production rates of CN and BO/CN-3 are evaluated to be 17.376 μmol L^{-1} h^{-1} and 11.268 μmol L^{-1} h^{-1} (Fig. S9b). Some literature has proved that another process relevant to the generation of singlet oxygen ($^1O_2$) is energy transfer [5, 6]. Based on the point, we further examine the steady-state phosphorescence (PH) spectra of CN and CN/BO-3. If the energy transfer process is suitable for BO/CN-3, the PH intensity can be enhanced compared to pristine CN. However, strong suppression signals were observed for BO/CN-3, suggesting the neglectable presence of triplet excitons during the reaction process (Fig. S10).

According to the above analysis and discussion, two possible heterojunctions were

proposed. As illustrated in Scheme 2a, under visible light illumination the photoinduced electrons migrated from the CB of CN to the CB of BO, while the remaining holes departed from the VB of BO to the VB of CN. However, compared to the standard redox potential of $O_2/\bullet O_2^-$(−0.33 eV vs NHE), the more positive CB edge potential of $Bi_2O_2CO_3$ was incapable to produce $\bullet O_2^-$ radicals [68]. Meanwhile, the photoinduced holes mainly located in the VB of g-C_3N_4, which possessed a weak potential for oxidizing organic pollutants or reacting with $\bullet O_2^-$. As a result, if $Bi_2O_2CO_3$/ g-C_3N_4 composites were type II photocatalytic systems, it was hard to detect strong $^1O_2$ and holes signals in EPR spin-trapping experiments. Conversely, Scheme 2b displayed a direct Z-scheme heterojunction. The evolution of the bandgap of $Bi_2O_2CO_3$/g-C_3N_4 heterojunctions suggested that $Bi_2O_2CO_3$ incorporated in porous g-C_3N_4 could positively modulate the bandgap of porous g-C_3N_4. At the interface between $Bi_2O_2CO_3$ and porous g-C_3N_4, the intimate contact and the doped N atoms escaping from g-C_3N_4 to $Bi_2O_2CO_3$ provided a charge transport chain [75]. In fact, theory calculation [39] has shown that $Bi_2O_2CO_3$ possess negative planar-averaged charge density at the contacted interface, while g-C_3N_4 showed a positive planar-averaged charge density. It indicated that g-C_3N_4 could accumulate electrons, while holes mainly gather in $Bi_2O_2CO_3$. Hence, the photoexcited electrons in the CB of $Bi_2O_2CO_3$ are more likely to transfer to the VB of g-C_3N_4 by means of the interfacial design under built-in electric field driving, whereas holes are stored at the VB of $Bi_2O_2CO_3$. Subsequently, the electron with strong reduction ability accumulating in the CB of g-C_3N_4 can efficiently react with O_2 to form $\bullet O_2^-$ and then further was oxidized to $^1O_2$, while the holes with high oxidation ability

in the VB of $Bi_2O_2CO_3$ could directly participate the reaction to degrade antibiotics. The above analysis is also well in accord with the EPR measurements. In summary, we suggest an all-solid-state Z-scheme is built after decorating $Bi_2O_2CO_3$, which efficiently drive the separation and transfer of charge pairs and enhance photocatalytic activity.

4 Conclusion

A Z-scheme system of $Bi_2O_2CO_3$/ porous g-C_3N_4 was fabricated via a bismuth-based MOFs derived strategy. Relying on the pre-treating process, the $Bi_2O_2CO_3$ were uniformly embedded into the surface, edge, and interlayers of g-C_3N_4, which efficiently enlarged the surface area and pore volume. Benefitting from the intimate contact at the interface and construction of a Z-scheme system, the photoinduced charge carriers of the heterojunctions can be significantly separated and transferred. As a result, $Bi_2O_2CO_3$/ g-C_3N_4 presented excellent photocatalytic activity and recyclability for the degradation of SMT, with nearly 6 times as high as that of porous g-C_3N_4 under visible light illumination. The mechanism analysis demonstrates that the $Bi_2O_2CO_3$-embedded porous g-C_3N_4 structural feature serves to selectively generate $^1O_2$ during the molecular oxygen activation. This work not only provides an approach to develop homogeneous $Bi_2O_2CO_3$/g-C_3N_4 heterostructures from a MOF-assisted route but also establishes a depth understanding of $^1O_2$ generation and their efforts on the promoted photocatalysis for efficient environment remediation.

Acknowledgments

This work was supported by the National Natural Science Foundation of China (No. 51709101, 51508177, 51579098, 51779090, 51521006), the National Program for

Support of Top-Notch Young Professionals of China (2014), Hunan Provincial Science and Technology Plan Project (No.2016RS3026, 2017SK2243), the Program for Changjiang Scholars and Innovative Research Team in University (IRT-13R17) and the Three Gorges Follow-up Research Project (2017HXXY-05).

References

[1] A. Karkman, K. Parnanen, D.G.J. Larsson, Fecal pollution can explain antibiotic resistance gene abundances in anthropogenically impacted environments, Nat. Commun., 10 (2019) 80.

[2] Y. Wang, Y. Zhu, Y. Hu, G. Zeng, Y. Zhang, C. Zhang, C. Feng, How to Construct DNA Hydrogels for Environmental Applications: Advanced Water Treatment and Environmental Analysis, Small, 14 (2018) e1703305.

[3] G. Li, X. Nie, J. Chen, P.K. Wong, T. An, H. Yamashita, H. Zhao, Enhanced simultaneous PEC eradication of bacteria and antibiotics by facilely fabricated high-activity {001} facets TiO_2 mounted onto TiO_2 nanotubular photoanode, Water Res., 101 (2016) 537-605.

[4] J. Wang, W. Zhang, J. Wei, Fabrication of poly(β-cyclodextrin)-conjugated magnetic graphene oxide by surface-initiated RAFT polymerization for synergetic adsorption of heavy metal ions and organic pollutants, J. Mater. Chem. A, 7 (2019) 2055-2065.

[5] P. Xu, G.M. Zeng, D.L. Huang, C.L. Feng, S. Hu, M.H. Zhao, C. Lai, Z. Wei, C. Huang, G.X. Xie, Z.F. Liu, Use of iron oxide nanomaterials in wastewater treatment: a review, Sci. Total. Environ., 424 (2012) 1-10.

[6] B. Song, M. Chen, S. Ye, P. Xu, G. Zeng, J. Gong, J. Li, P. Zhang, W. Cao, Effects of multi-walled carbon nanotubes on metabolic function of the microbial community in riverine sediment contaminated with phenanthrene, Carbon, 144 (2019) 1-7.

[7] L. Zhang, J. Zhang, G. Zeng, H. Dong, Y. Chen, C. Huang, Y. Zhu, R. Xu, Y. Cheng, K. Hou, W. Cao, W. Fang, Multivariate relationships between microbial communities and environmental variables during co-composting of sewage sludge and agricultural waste in the presence of PVP-AgNPs, Bioresour Technol, 261 (2018) 10-18.

[8] B. Shao, Z. Liu, G. Zeng, Z. Wu, Y. Liu, M. Cheng, M. Chen, Y. Liu, W. Zhang, H. Feng, Nitrogen-Doped Hollow Mesoporous Carbon Spheres Modified g-C_3N_4/Bi_2O_3 Direct Dual Semiconductor Photocatalytic System with Enhanced Antibiotics Degradation under Visible Light, ACS Sustainable. Chem. Eng., 6 (2018) 16424-16436.

[9] S. Tian, C. Zhang, D. Huang, R. Wang, G. Zeng, M. Yan, W. Xiong, C. Zhou, M. Cheng, W. Xue, Y. Yang, W. Wang, Recent progress in sustainable technologies for adsorptive and reactive removal of sulfonamides, Chem. Eng. J., (2019).

[10] M.C. DeRosa, R.J. Crutchley, Photosensitized singlet oxygen and its applications, Coord. Chem. Rev., 233 (2002) 351-371.

[11] H. Wang, Z. Zeng, P. Xu, L. Li, G. Zeng, R. Xiao, Z. Tang, D. Huang, L. Tang, C. Lai, D. Jiang, Y. Liu, H. Yi, L. Qin, S. Ye, X. Ren, W. Tang, Recent progress in covalent organic framework thin films: fabrications, applications and perspectives, Chem Soc Rev, 48 (2019) 488-516.

[12] C. Zhou, C. Lai, C. Zhang, G. Zeng, D. Huang, M. Cheng, L. Hu, W. Xiong, M. Chen, J. Wang, Y. Yang, L. Jiang, Semiconductor/boron nitride composites: Synthesis, properties, and photocatalysis applications, Appl. Catal., B, 238 (2018) 6-18.

[13] X. Wang, K. Maeda, A. Thomas, K. Takanabe, G. Xin, J.M. Carlsson, K. Domen, M. Antonietti, A metal-free polymeric photocatalyst for hydrogen production from water under visible light, Nat. Mater., 8 (2009) 76-80.

[14] Y. Yang, Z. Zeng, G. Zeng, D. Huang, R. Xiao, C. Zhang, C. Zhou, W. Xiong, W. Wang, M. Cheng, W. Xue, H. Guo, X. Tang, D. He, Ti_3C_2 Mxene/porous g-C_3N_4 interfacial Schottky junction for boosting spatial charge separation in photocatalytic H_2O_2 production, Appl. Catal., B, 258 (2019).

[15] D. He, C. Zhang, G. Zeng, Y. Yang, D. Huang, L. Wang, H. Wang, A multifunctional platform

by controlling of carbon nitride in the core-shell structure: From design to construction, and catalysis applications, Appl. Catal., B, 258 (2019) 117957.

[16] H. Wang, X. Sun, D. Li, X. Zhang, S. Chen, W. Shao, Y. Tian, Y. Xie, Boosting Hot-Electron Generation: Exciton Dissociation at the Order-Disorder Interfaces in Polymeric Photocatalysts, J. Am. Chem. Soc., 139 (2017) 2468-2473.

[17] L. Yang, X. Bai, J. Shi, X. Du, L. Xu, P. Jin, Quasi-full-visible-light absorption by D35-TiO_2/g-C_3N_4 for synergistic persulfate activation towards efficient photodegradation of micropollutants, Appl. Catal., B, 256 (2019).

[18] Y. Chen, J. Zhang, M. Zhang, X. Wang, Molecular and textural engineering of conjugated carbon nitride catalysts for selective oxidation of alcohols with visible light, Chem. Sci., 4 (2013).

[19] C. Zhou, C. Lai, D. Huang, G. Zeng, C. Zhang, M. Cheng, L. Hu, J. Wan, W. Xiong, M. Wen, X. Wen, L. Qin, Highly porous carbon nitride by supramolecular preassembly of monomers for photocatalytic removal of sulfamethazine under visible light driven, Appl. Catal., B, 220 (2018) 202-210.

[20] Q. Han, Z. Cheng, B. Wang, H. Zhang, L. Qu, Significant Enhancement of Visible-Light-Driven Hydrogen Evolution by Structure Regulation of Carbon Nitrides, ACS Nano, 12 (2018) 5221-5227.

[21] J. Wu, N. Li, X.-H. Zhang, H.-B. Fang, Y.-Z. Zheng, X. Tao, Heteroatoms binary-doped hierarchical porous g-C_3N_4 nanobelts for remarkably enhanced visible-light-driven hydrogen evolution, Appl. Catal., B, 226 (2018) 61-70.

[22] Z.-F. Huang, J. Song, L. Pan, Z. Wang, X. Zhang, J.-J. Zou, W. Mi, X. Zhang, L. Wang, Carbon nitride with simultaneous porous network and O-doping for efficient solar-energy-driven hydrogen

602 evolution, Nano Energy, 12 (2015) 646-656.

603 [23] M. Wang, P. Guo, Y. Zhang, C. Lv, T. Liu, T. Chai, Y. Xie, Y. Wang, T. Zhu, Synthesis of hollow

604 lantern-like Eu(III)-doped g-C_3N_4 with enhanced visible light photocatalytic perfomance for organic

605 degradation, J. Hazard. Mater., 349 (2018) 224-233.

606 [24] H. Yu, R. Shi, Y. Zhao, T. Bian, Y. Zhao, C. Zhou, G.I.N. Waterhouse, L.Z. Wu, C.H. Tung, T.

607 Zhang, Alkali-Assisted Synthesis of Nitrogen Deficient Graphitic Carbon Nitride with Tunable

608 Band Structures for Efficient Visible-Light-Driven Hydrogen Evolution, Adv. Mater., 29 (2017).

609 [25] W.-J. Ong, L.K. Putri, Y.-C. Tan, L.-L. Tan, N. Li, Y.H. Ng, X. Wen, S.-P. Chai, Unravelling

610 charge carrier dynamics in protonated g-C_3N_4 interfaced with carbon nanodots as co-catalysts

611 toward enhanced photocatalytic CO_2 reduction: A combined experimental and first-principles DFT

612 study, Nano Res., 10 (2017) 1673-1696.

613 [26] P. Suyana, P. Ganguly, B.N. Nair, A.P. Mohamed, K.G.K. Warrier, U.S. Hareesh, Co_3O_4–C_3N_4

614 p–n nano-heterojunctions for the simultaneous degradation of a mixture of pollutants under solar

615 irradiation, Environmental Science: Nano, 4 (2017) 212-221.

616 [27] Y. Yang, C. Zhang, D. Huang, G. Zeng, J. Huang, C. Lai, C. Zhou, W. Wang, H. Guo, W. Xue,

617 R. Deng, M. Cheng, W. Xiong, Boron nitride quantum dots decorated ultrathin porous g-C_3N_4:

618 Intensified exciton dissociation and charge transfer for promoting visible-light-driven molecular

619 oxygen activation, Appl. Catal., B, 245 (2019) 87-99.

620 [28] R. Abazari, A.R. Mahjoub, G. Salehi, Preparation of amine functionalized g-C_3N_4@$^{(H/S)}$MOF

621 NCs with visible light photocatalytic characteristic for 4-nitrophenol degradation from aqueous

622 solution, J. Hazard. Mater., 365 (2019) 921-931.

623 [29] J. Low, B. Dai, T. Tong, C. Jiang, J. Yu, In Situ Irradiated X-Ray Photoelectron Spectroscopy

624 Investigation on a Direct Z-Scheme TiO_2 /CdS Composite Film Photocatalyst, Adv. Mater., 31
625 (2019) e1802981.
626 [30] D. Huang, S. Chen, G. Zeng, X. Gong, C. Zhou, M. Cheng, W. Xue, X. Yan, J. Li, Artificial Z-
627 scheme photocatalytic system: What have been done and where to go?, Coord. Chem. Rev., 385
628 (2019) 44-80.
629 [31] H. Li, F. Deng, Y. Zheng, L. Hua, C. Qu, X. Luo, Visible-light-driven Z-scheme rGO/Bi_2S_3–
630 BiOBr heterojunctions with tunable exposed BiOBr (102) facets for efficient synchronous
631 photocatalytic degradation of 2-nitrophenol and Cr(vi) reduction, Environ. Sci. Nano, 6 (2019)
632 3670-3683.
633 [32] W. Shan, Y. Hu, Z. Bai, M. Zheng, C. Wei, In situ preparation of g-C_3N_4 /bismuth-based oxide
634 nanocomposites with enhanced photocatalytic activity, Appl. Catal., B, 188 (2016) 1-12.
635 [33] H. Zhao, G. Li, F. Tian, Q. Jia, Y. Liu, R. Chen, g-C_3N_4 surface-decorated $Bi_2O_2CO_3$ for
636 improved photocatalytic performance: Theoretical calculation and photodegradation of antibiotics
637 in actual water matrix, Chem. Eur. J., 366 (2019) 468-479.
638 [34] M. Xiong, L. Chen, C. Yuan, J. He, S.-L. Luo, C.-T. Au, S.-F. Yin, Controlled synthesis of
639 graphitic carbon nitride/beta bismuth oxide composite and its high visible-light photocatalytic
640 activity, Carbon, 86 (2015) 217-224.
641 [35] Q. Zhang, H. Wang, S. Hu, G. Lu, J. Bai, X. Kang, D. Liu, J. Gui, Synthesis and properties of
642 visible light responsive g-C_3N_4/$Bi_2O_2CO_3$ layered heterojunction nanocomposites, RSC Adv., 5
643 (2015) 42736-42743.
644 [36] Q. Zhang, S. Yuan, B. Xu, Y. Xu, K. Cao, Z. Jin, C. Qiu, M. Zhang, C. Su, T. Ohno, A facile
645 approach to build $Bi_2O_2CO_3$/PCN nanohybrid photocatalysts for gaseous acetaldehyde efficient

removal, Catalysis Today, 315 (2018) 184-193.

[37] X. Zhao, J. Feng, J. Liu, J. Lu, W. Shi, G. Yang, G. Wang, P. Feng, P. Cheng, Metal-Organic Framework-Derived ZnO/ZnS Heteronanostructures for Efficient Visible-Light-Driven Photocatalytic Hydrogen Production, Adv. Sci. (Weinh), 5 (2018) 1700590.

[38] Z. Wang, Y. Huang, W. Ho, J. Cao, Z. Shen, S.C. Lee, Fabrication of $Bi_2O_2CO_3$/g-C_3N_4 heterojunctions for efficiently photocatalytic NO in air removal: In-situ self-sacrificial synthesis, characterizations and mechanistic study, Appl. Catal., B, 199 (2016) 123-133.

[39] C. Yang, Z. Xue, J. Qin, M. Sawangphruk, S. Rajendran, X. Zhang, R. Liu, Visible Light-Driven Photocatalytic H_2 Generation and Mechanism Insights into $Bi_2O_2CO_3$/G-C_3N_4 Z-Scheme Photocatalyst, J. Phys. Chem. C, 123 (2019) 4795-4804.

[40] K. Wang, Y. Li, G. Zhang, J. Li, X. Wu, 0D Bi nanodots/2D Bi_3NbO_7 nanosheets heterojunctions for efficient visible light photocatalytic degradation of antibiotics: Enhanced molecular oxygen activation and mechanism insight, Appl. Catal., B, 240 (2019) 39-49.

[41] H. Wang, D. Yong, S. Chen, S. Jiang, X. Zhang, W. Shao, Q. Zhang, W. Yan, B. Pan, Y. Xie, Oxygen-Vacancy-Mediated Exciton Dissociation in BiOBr for Boosting Charge-Carrier-Involved Molecular Oxygen Activation, J. Am. Chem. Soc., 140 (2018) 1760-1766.

[42] S. Dang, Q.-L. Zhu, Q. Xu, Nanomaterials derived from metal–organic frameworks, Nat. Rev. Mater., 3 (2017).

[43] D. Jiang, M. Chen, H. Wang, G. Zeng, D. Huang, M. Cheng, Y. Liu, W. Xue, Z. Wang, The application of different typological and structural MOFs-based materials for the dyes adsorption, Coord. Chem. Rev., 380 (2019) 471-483.

[44] W. Xiong, Z. Zeng, X. Li, G. Zeng, R. Xiao, Z. Yang, Y. Zhou, C. Zhang, M. Cheng, L. Hu, C.

668 Zhou, L. Qin, R. Xu, Y. Zhang, Multi-walled carbon nanotube/amino-functionalized MIL-53(Fe)
669 composites: Remarkable adsorptive removal of antibiotics from aqueous solutions, Chemosphere,
670 210 (2018) 1061-1069.
671 [45] X. Tang, G. Zeng, C. Fan, M. Zhou, L. Tang, J. Zhu, J. Wan, D. Huang, M. Chen, P. Xu, C.
672 Zhang, Y. Lu, W. Xiong, Chromosomal expression of CadR on Pseudomonas aeruginosa for the
673 removal of Cd(II) from aqueous solutions, Sci. Total. Environ., 636 (2018) 1355-1361.
674 [46] M. Feyand, E. Mugnaioli, F. Vermoortele, B. Bueken, J.M. Dieterich, T. Reimer, U. Kolb, D.
675 de Vos, N. Stock, Automated diffraction tomography for the structure elucidation of twinned, sub-
676 micrometer crystals of a highly porous, catalytically active bismuth metal-organic framework,
677 Angew. Chem. Int. Ed., 51 (2012) 10373-10376.
678 [47] M. Savage, S. Yang, M. Suyetin, E. Bichoutskaia, W. Lewis, A.J. Blake, S.A. Barnett, M.
679 Schroder, A novel bismuth-based metal-organic framework for high volumetric methane and carbon
680 dioxide adsorption, Chemistry, 20 (2014) 8024-8029.
681 [48] A.K. Inge, M. Koppen, J. Su, M. Feyand, H. Xu, X. Zou, M. O'Keeffe, N. Stock, Unprecedented
682 Topological Complexity in a Metal-Organic Framework Constructed from Simple Building Units,
683 J. Am. Chem. Soc., 138 (2016) 1970-1976.
684 [49] M. Koppen, O. Beyer, S. Wuttke, U. Luning, N. Stock, Synthesis, functionalisation and post-
685 synthetic modification of bismuth metal-organic frameworks, Dalton Trans., 46 (2017) 8658-8663.
686 [50] M. Köppen, A. Dhakshinamoorthy, A.K. Inge, O. Cheung, J. Ångström, P. Mayer, N. Stock,
687 Synthesis, Transformation, Catalysis, and Gas Sorption Investigations on the Bismuth Metal–
688 Organic Framework CAU-17, Eur. J. Inorg. Chem., 2018 (2018) 3496-3503.
689 [51] H. Ouyang, N. Chen, G. Chang, X. Zhao, Y. Sun, S. Chen, H. Zhang, D. Yang, Selective

690 Capture of Toxic Selenite Anions by Bismuth-based Metal-Organic Frameworks, Angew. Chem.
691 Int. Ed., 57 (2018) 13197-13201.
692 [52] E. Zhang, T. Wang, K. Yu, J. Liu, W. Chen, A. Li, H. Rong, R. Lin, S. Ji, X. Zheng, Y. Wang,
693 L. Zheng, C. Chen, D. Wang, J. Zhang, Y. Li, Bismuth Single Atoms Resulting from Transformation
694 of Metal-Organic Frameworks and Their Use as Electrocatalysts for CO_2 Reduction, J. Am. Chem.
695 Soc., 141 (2019) 16569-16573.
696 [53] K. Xiao, T. Wang, M. Sun, A. Hanif, Q. Gu, B. Tian, Z. Jiang, B. Wang, H. Sun, J. Shang, P.K.
697 Wong, Photocatalytic Bacterial Inactivation by a Rape Pollen-MoS_2 Biohybrid Catalyst: Synergetic
698 Effects and Inactivation Mechanisms, Environ. Sci. Technol., (2019).
699 [54] Y. Zeng, X. Liu, C. Liu, L. Wang, Y. Xia, S. Zhang, S. Luo, Y. Pei, Scalable one-step production
700 of porous oxygen-doped g-C_3N_4 nanorods with effective electron separation for excellent visible-
701 light photocatalytic activity, Appl. Catal., B, 224 (2018) 1-9.
702 [55] L. Yang, J. Huang, L. Shi, L. Cao, Q. Yu, Y. He, J. Fei, H. Ouyang, J. Ye, A surface modification
703 resultant thermally oxidized porous g-C_3N_4 with enhanced photocatalytic hydrogen production,
704 Appl. Catal., B, 204 (2017) 335-345.
705 [56] Y. Gao, Y. Zhu, L. Lyu, Q. Zeng, X. Xing, C. Hu, Electronic Structure Modulation of Graphitic
706 Carbon Nitride by Oxygen Doping for Enhanced Catalytic Degradation of Organic Pollutants
707 through Peroxymonosulfate Activation, Environ. Sci. Technol., 52 (2018) 14371-14380.
708 [57] W. Wang, P. Xu, M. Chen, G. Zeng, C. Zhang, C. Zhou, Y. Yang, D. Huang, C. Lai, M. Cheng,
709 L. Hu, W. Xiong, H. Guo, M. Zhou, Alkali Metal-Assisted Synthesis of Graphite Carbon Nitride
710 with Tunable Band-Gap for Enhanced Visible-Light-Driven Photocatalytic Performance, ACS
711 Sustainable. Chem. Eng., 6 (2018) 15503-15516.

712 [58] Z. Zhao, Y. Zhou, F. Wang, K. Zhang, S. Yu, K. Cao, Polyaniline-decorated {001} facets of
713 $Bi_2O_2CO_3$ nanosheets: in situ oxygen vacancy formation and enhanced visible light photocatalytic
714 activity, ACS Appl. Mater. Interfaces, 7 (2015) 730-737.
715 [59] Y. Li, Y. Fang, Z. Cao, N. Li, D. Chen, Q. Xu, J. Lu, Construction of g-C_3N_4/PDI@MOF
716 heterojunctions for the highly efficient visible light-driven degradation of pharmaceutical and
717 phenolic micropollutants, Appl. Catal., B, 250 (2019) 150-162.
718 [60] M. Cheng, C. Lai, Y. Liu, G. Zeng, D. Huang, C. Zhang, L. Qin, L. Hu, C. Zhou, W. Xiong,
719 Metal-organic frameworks for highly efficient heterogeneous Fenton-like catalysis, Coord. Chem.
720 Rev., 368 (2018) 80-92.
721 [61] Z. Jiang, H. Sun, T. Wang, B. Wang, W. Wei, H. Li, S. Yuan, T. An, H. Zhao, J. Yu, P.K. Wong,
722 Nature-based catalyst for visible-light-driven photocatalytic CO_2 reduction, Energy Environ. Sci.,
723 11 (2018) 2382-2389.
724 [62] G. Salehi, R. Abazari, A.R. Mahjoub, Visible-Light-Induced Graphitic-C_3N_4@Nickel-
725 Aluminum Layered Double Hydroxide Nanocomposites with Enhanced Photocatalytic Activity for
726 Removal of Dyes in Water, Inorg Chem, 57 (2018) 8681-8691.
727 [63] J. Li, G. Zhan, Y. Yu, L. Zhang, Superior visible light hydrogen evolution of Janus bilayer
728 junctions via atomic-level charge flow steering, Nat Commun, 7 (2016) 11480.
729 [64] X. Chen, G. Fang, C. Liu, D.D. Dionysiou, X. Wang, C. Zhu, Y. Wang, J. Gao, D. Zhou,
730 Cotransformation of Carbon Dots and Contaminant under Light in Aqueous Solutions: A
731 Mechanistic Study, Environ. Sci. Technol., 53 (2019) 6235-6244.
732 [65] C.-C. Wang, J.-R. Li, X.-L. Lv, Y.-Q. Zhang, G. Guo, Photocatalytic organic pollutants
733 degradation in metal–organic frameworks, Energy Environ. Sci., 7 (2014) 2831-2867.

734 [66] J.L. Gong, B. Wang, G.M. Zeng, C.P. Yang, C.G. Niu, Q.Y. Niu, W.J. Zhou, Y. Liang, Removal
735 of cationic dyes from aqueous solution using magnetic multi-wall carbon nanotube nanocomposite
736 as adsorbent, J. Hazard. Mater., 164 (2009) 1517-1522.
737 [67] S.J. Ye, G.M. Zeng, H.P. Wu, C. Zhang, J. Dai, J. Liang, J.F. Yu, X.Y. Ren, H. Yi, M. Cheng,
738 C. Zhang, Biological technologies for the remediation of co-contaminated soil, Crit. Rev.
739 Biotechnol., 37 (2017) 1062-1076.
740 [68] C. Zhou, C. Lai, P. Xu, G. Zeng, D. Huang, C. Zhang, M. Cheng, L. Hu, J. Wan, Y. Liu, W.
741 Xiong, Y. Deng, M. Wen, In Situ Grown AgI/$Bi_{12}O_{17}Cl_2$ Heterojunction Photocatalysts for Visible
742 Light Degradation of Sulfamethazine: Efficiency, Pathway, and Mechanism, ACS Sustainable.
743 Chem. Eng., 6 (2018) 4174-4184.
744 [69] W. Fu, B. Li, J. Yang, H. Yi, L. Chai, X. Li, New insights into the chlorination of sulfonamide:
745 Smiles-type rearrangement, desulfation, and product toxicity, Chem. Eng. J., 331 (2018) 785-793.
746 [70] P. Zhang, X. Tan, S. Liu, Y. Liu, G. Zeng, S. Ye, Z. Yin, X. Hu, N. Liu, Catalytic degradation
747 of estrogen by persulfate activated with iron-doped graphitic biochar: Process variables effects and
748 matrix effects, Chem. Eur. J., 378 (2019).
749 [71] Y. Bai, X. Shi, P. Wang, L. Wang, H. Xie, Z. Li, L. Qu, L. Ye, Synthesis of one-dimensional
750 $Bi_5O_7Br_{0.5}I_{0.5}$ solid solution for effective real oilfield wastewater treatment via exciton
751 photocatalytic process, J. Taiwan. Inst. Chem. E, 91 (2018) 358-368.
752 [72] A.V. Demyanenko, A.S. Bogomolov, N.V. Dozmorov, A.I. Svyatova, A.P. Pyryaeva, V.G.
753 Goldort, S.A. Kochubei, A.V. Baklanov, Singlet Oxygen $^1O_2$ in Photocatalysis on TiO_2. Where Does
754 It Come from?, J. Phys. Chem. C, 123 (2019) 2175-2181.
755 [73] H. Wang, S. Jiang, S. Chen, D. Li, X. Zhang, W. Shao, X. Sun, J. Xie, Z. Zhao, Q. Zhang, Y.

Tian, Y. Xie, Enhanced Singlet Oxygen Generation in Oxidized Graphitic Carbon Nitride for Organic Synthesis, Adv. Mater., 28 (2016) 6940-6945.

[74] M. Moradi, G. Moussavi, K. Yaghmaeian, A. Yazdanbakhsh, V. Srivastava, M. Sillanpää, Synthesis of novel Ag-doped S-MgO nanosphere as an efficient UVA/LED-activated photocatalyst for non-radical oxidation of diclofenac: Catalyst preparation and characterization and photocatalytic mechanistic evaluation, Appl. Catal., B, 260 (2020).

[75] N. Li, Y. Ding, J. Wu, Z. Zhao, X. Li, Y.Z. Zheng, M. Huang, X. Tao, Efficient, Full Spectrum-Driven H_2 Evolution Z-Scheme Co_2P/CdS Photocatalysts with Co-S Bonds, ACS Appl. Mater. Interfaces, 11 (2019) 22297-22306.

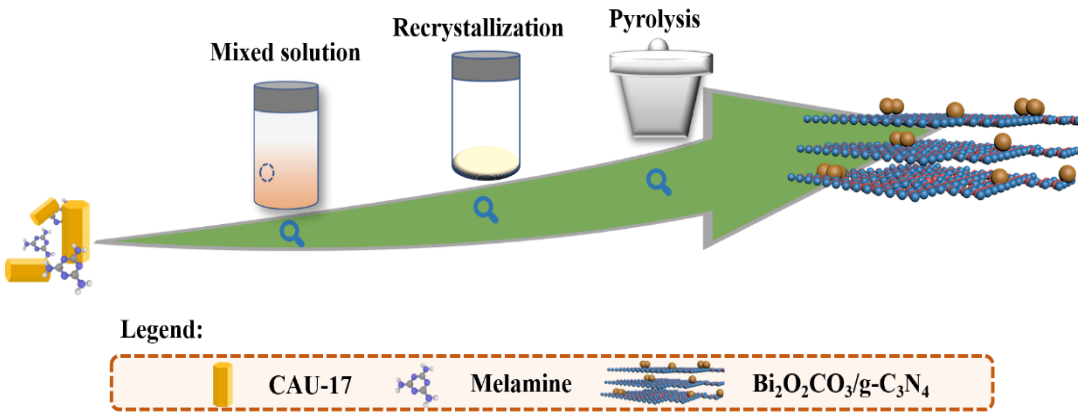

Scheme1. Process of the formation of $Bi_2O_2CO_3$/g-C_3N_4 composites.

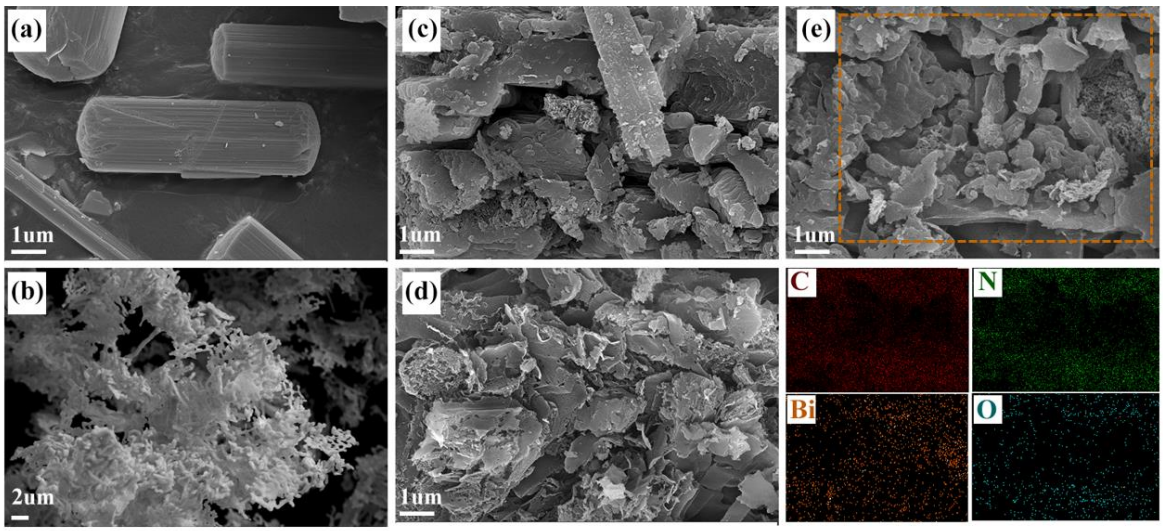

Fig. 1 SEM images of CAU-17 (a), Bi_2O_3 (b), g-C_3N_4 (c), $Bi_2O_2CO_3$/g-C_3N_4 (d-e), and SEM-EDS element mapping for $Bi_2O_2CO_3$/g-C_3N_4 corresponding to figure (e).

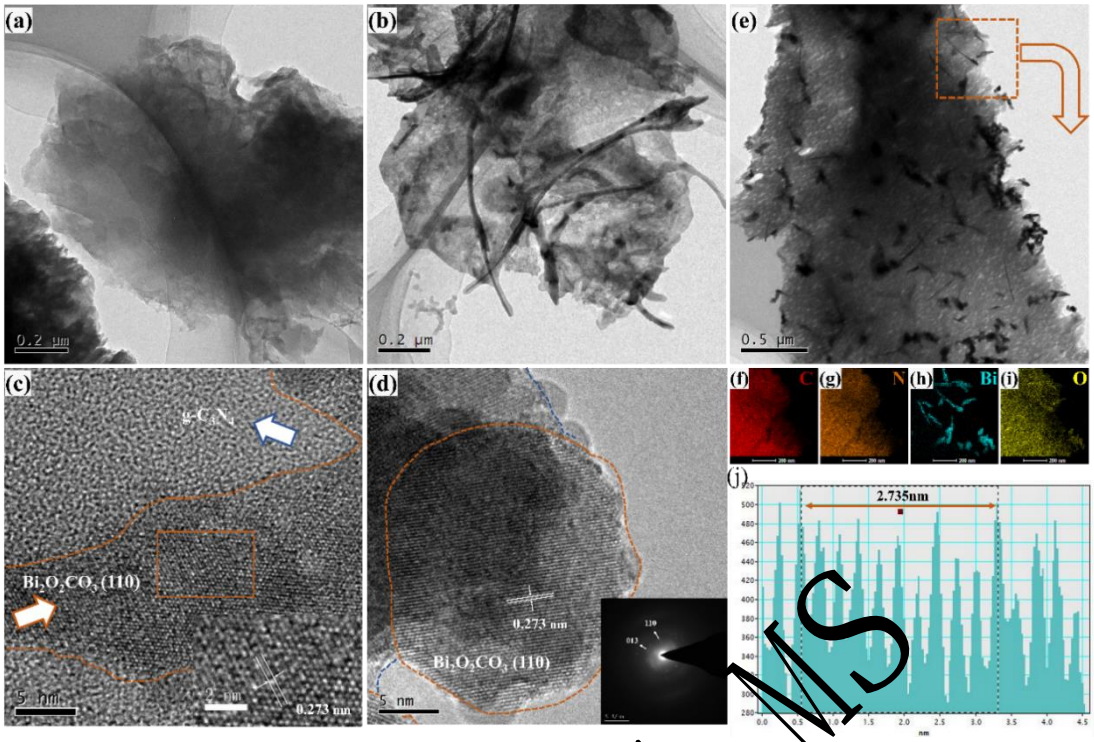

774

775 **Fig. 2** TEM images of g-C_3N_4 (a), $Bi_2O_2CO_3$/g-C_3N_4 (b and e). HRTEM image and selected area

776 electron diffraction image of $Bi_2O_2CO_3$/g-C_3N_4 (c, d) and HAADF-STEM images of (f) carbon, (g)

777 nitrogen, (h) oxygen and (i) bismuth. (j) Intensity profiles along the dotted line indicated in the

778 image.

779

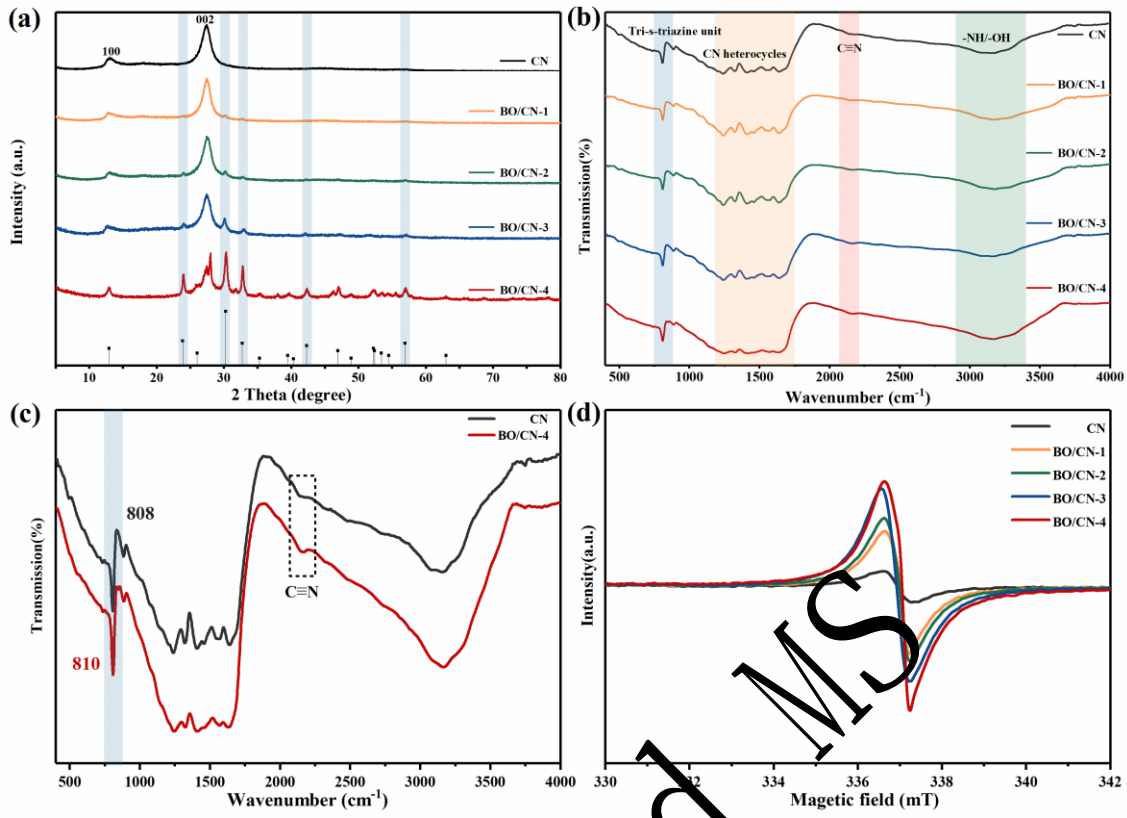

Fig. 3 (a) XRD patterns of pristine g-C_3N_4 and all of the $Bi_2O_2CO_3$/g-C_3N_4 composites. (b) FTIR spectra of pristine g-C_3N_4 and all of the $Bi_2O_2CO_3$/g-C_3N_4 composites. (c) Compared FTIR spectra of pristine g-C_3N_4 and BO/CN-4 (d) Room-temperature EPR signals of pristine g-C_3N_4 and all of the $Bi_2O_2CO_3$/g-C_3N_4 composites.

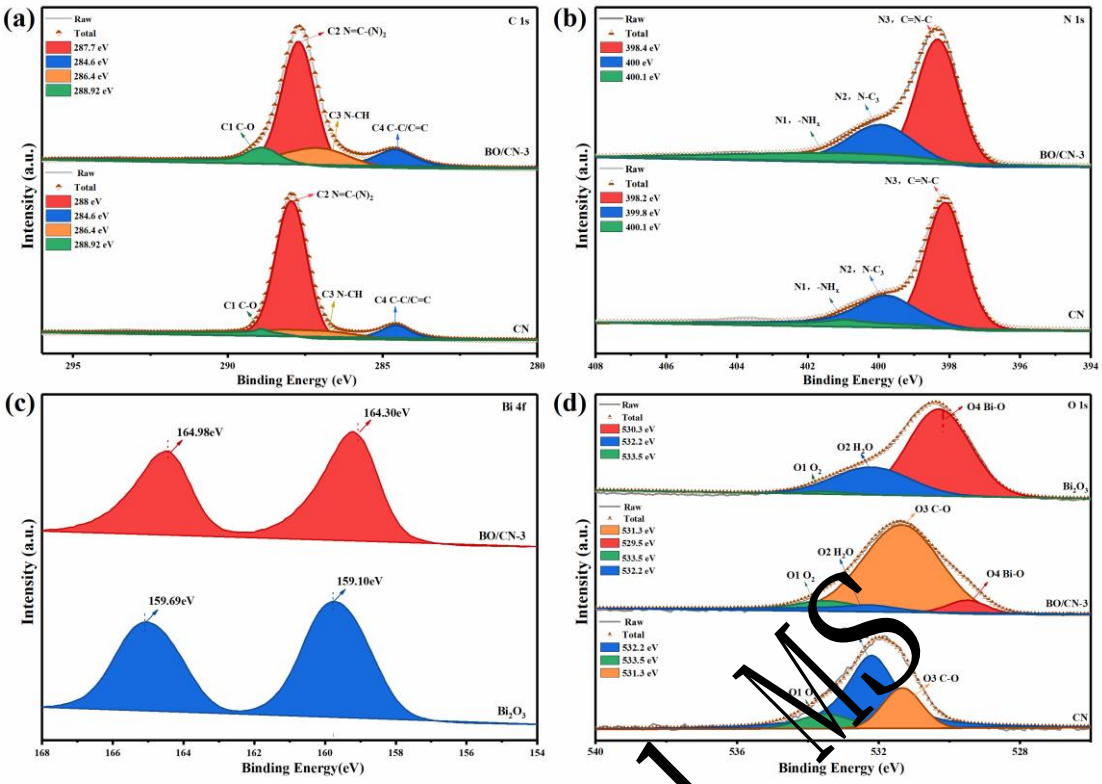

786

787 **Fig. 4** XPS spectra of pristine g-C_3N_4, Bi_2O_3 and the $Bi_2O_2CO_3$/g-C_3N_4 composites. (a) C 1s, (b) N

788 1s, (c) Bi 4f and (d) O 1s.

789

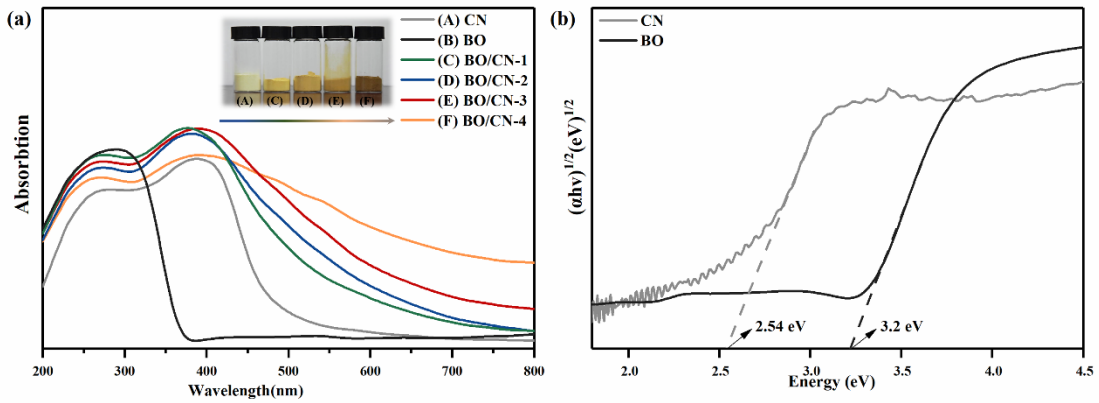

Fig. 5 (a) UV–vis DRS of pristine g-C_3N_4, $Bi_2O_2CO_3$, and $Bi_2O_2CO_3$/g-C_3N_4 composites. (b) Plots of transformed Kubelka–Munk function versus photon energy for g-C_3N_4, and $Bi_2O_2CO_3$.

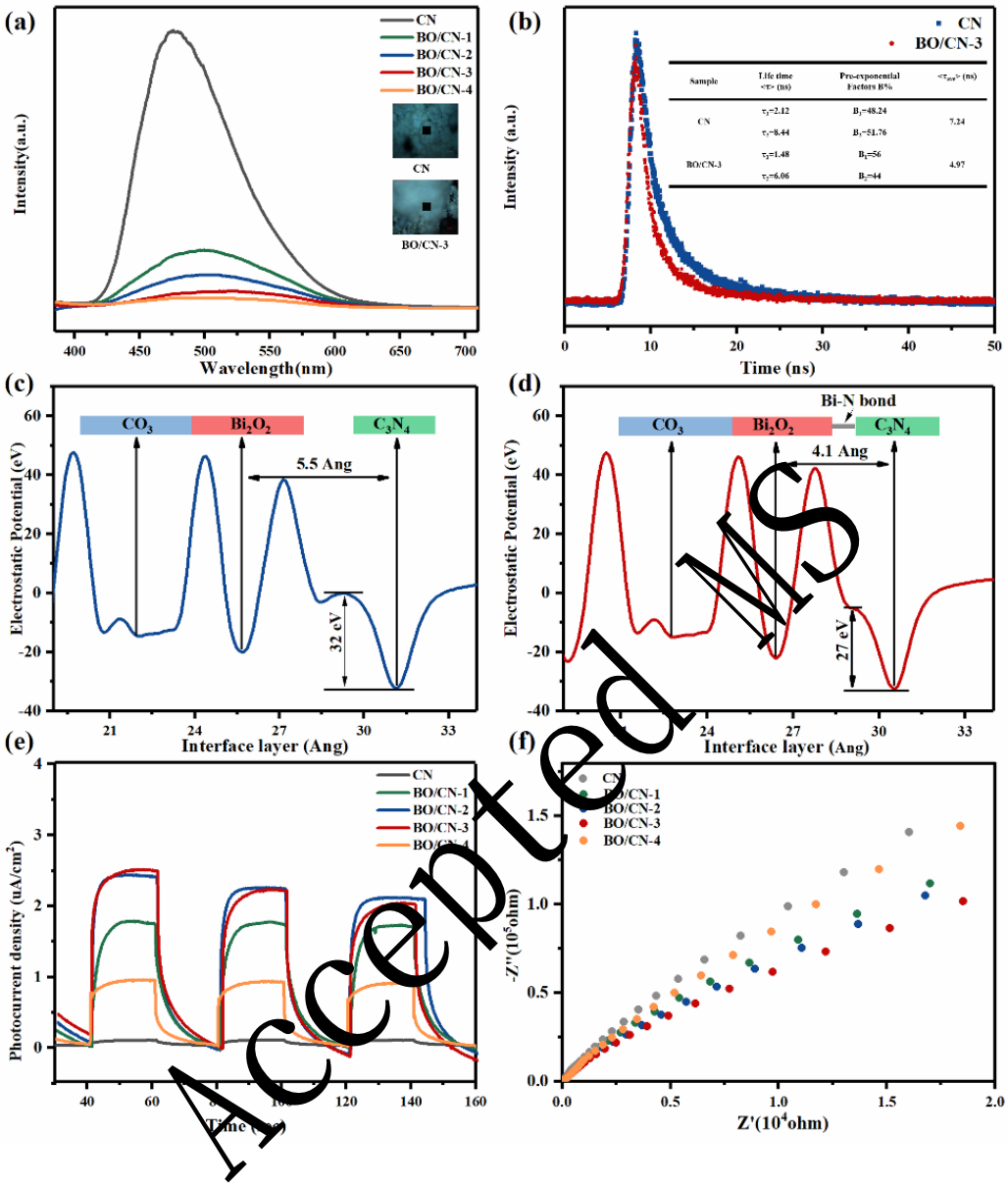

Fig. 6 (a) Steady-state PF spectra for pristine g-C_3N_4 and $Bi_2O_2CO_3$/g-C_3N_4 composites (300K). (b) Time-resolved PF spectra of pristine g-C_3N_4 and $Bi_2O_2CO_3$/g-C_3N_4 composites (excitation at 365nm). Comparison of the electrostatic potentials of BO/CN without (c) and with (d) Bi–N bonds. (e) Nyquist plots of electrochemical impedance spectroscopy. (f) Transient photocurrent response curves.

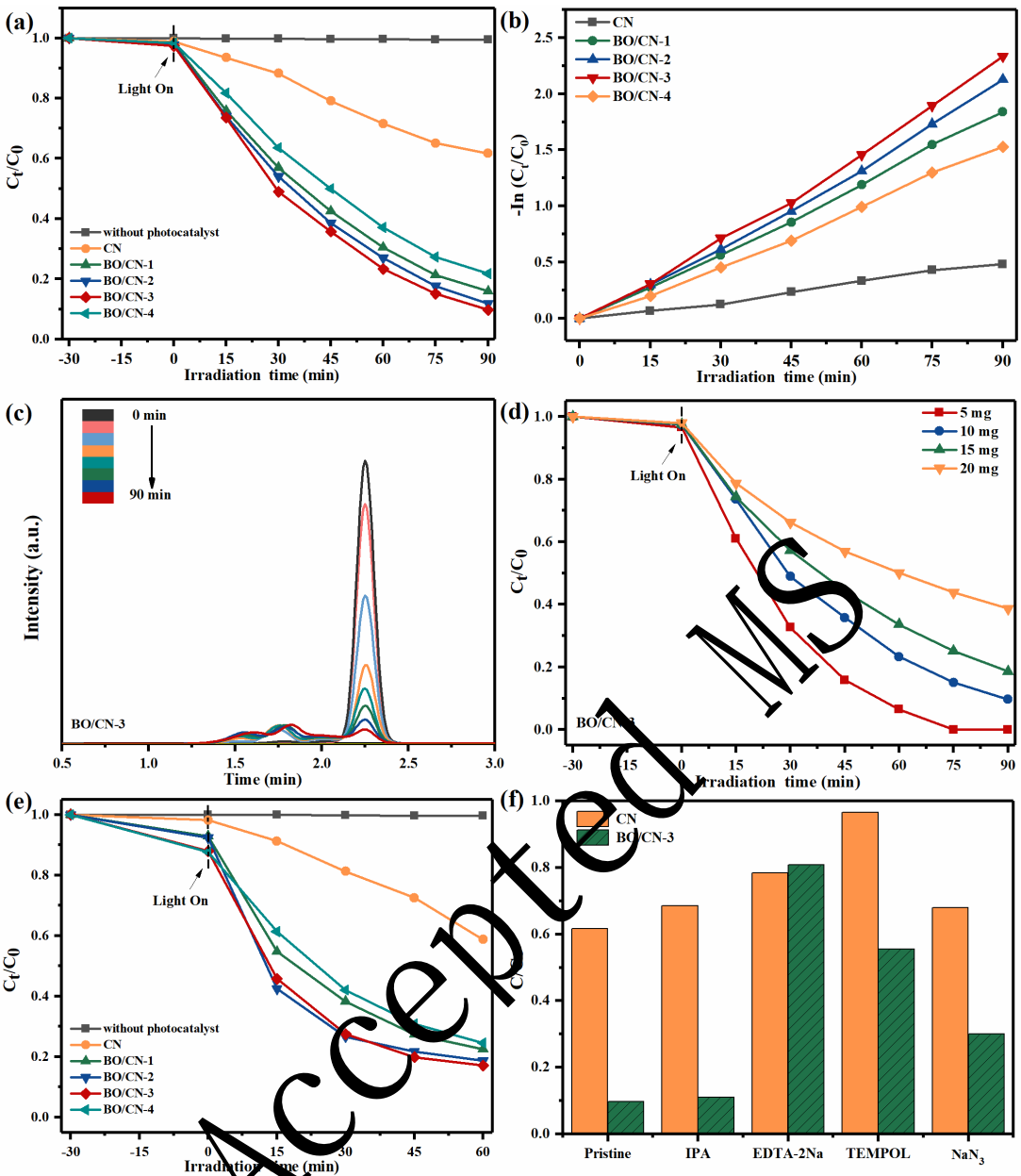

Fig. 7 (a) Photocatalytic degradation curves of SMT under visible light irradiation (λ > 420 nm) for different samples. (b) Pseudo-first-order kinetic fitting curves and the corresponding apparent rate constants (k). (c) HPLC chromatogram at various reaction times (d) Degradation activity of $Bi_2O_2CO_3$/g-C_3N_4 composites for different concentrations of SMT. (e) Photocatalytic degradation curves of TC under visible light irradiation (λ > 420 nm) for different samples. (f) Effect of different quench agents on photocatalytic degradation of SMT by $Bi_2O_2CO_3$/g-C_3N_4 composites.

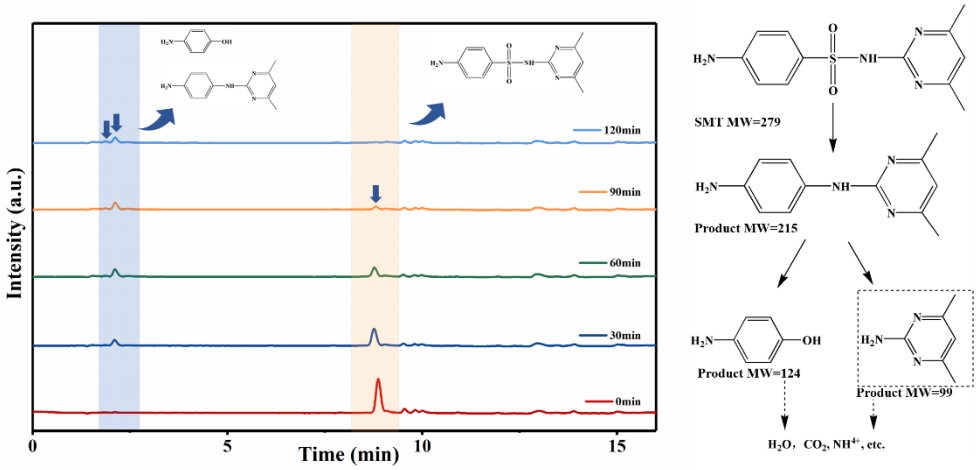

Figure. 8 (a) HPLC/MS scan spectra of the intermediates detected in the degradation of SMT. (b) The proposed degradation pathways of SMT in this system.

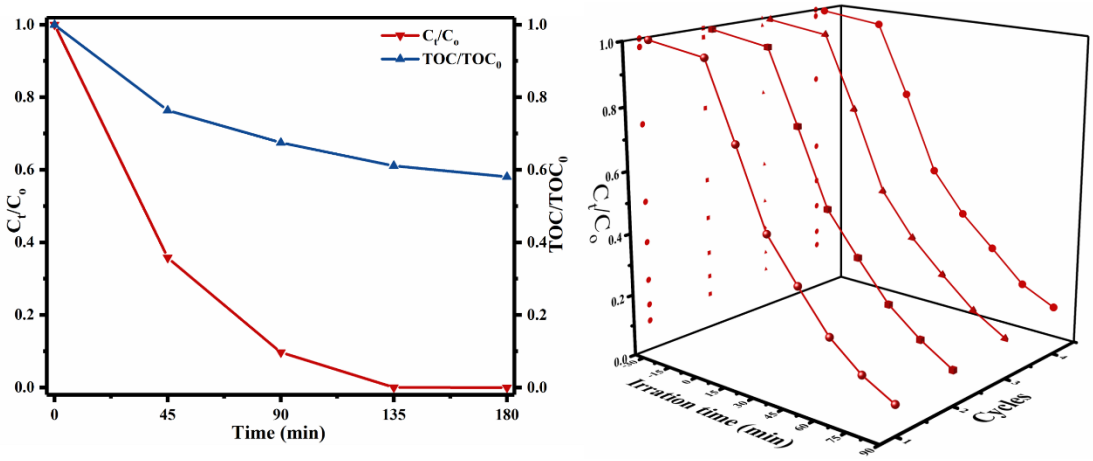

814

815 **Figure. 9** (a) The photodegradation and TOC removal curves of SMT on BO/CN-3 composites. (b)

816 The cycling runs in the photodegradation of SMT over BO/CN-3 composites.

817

818

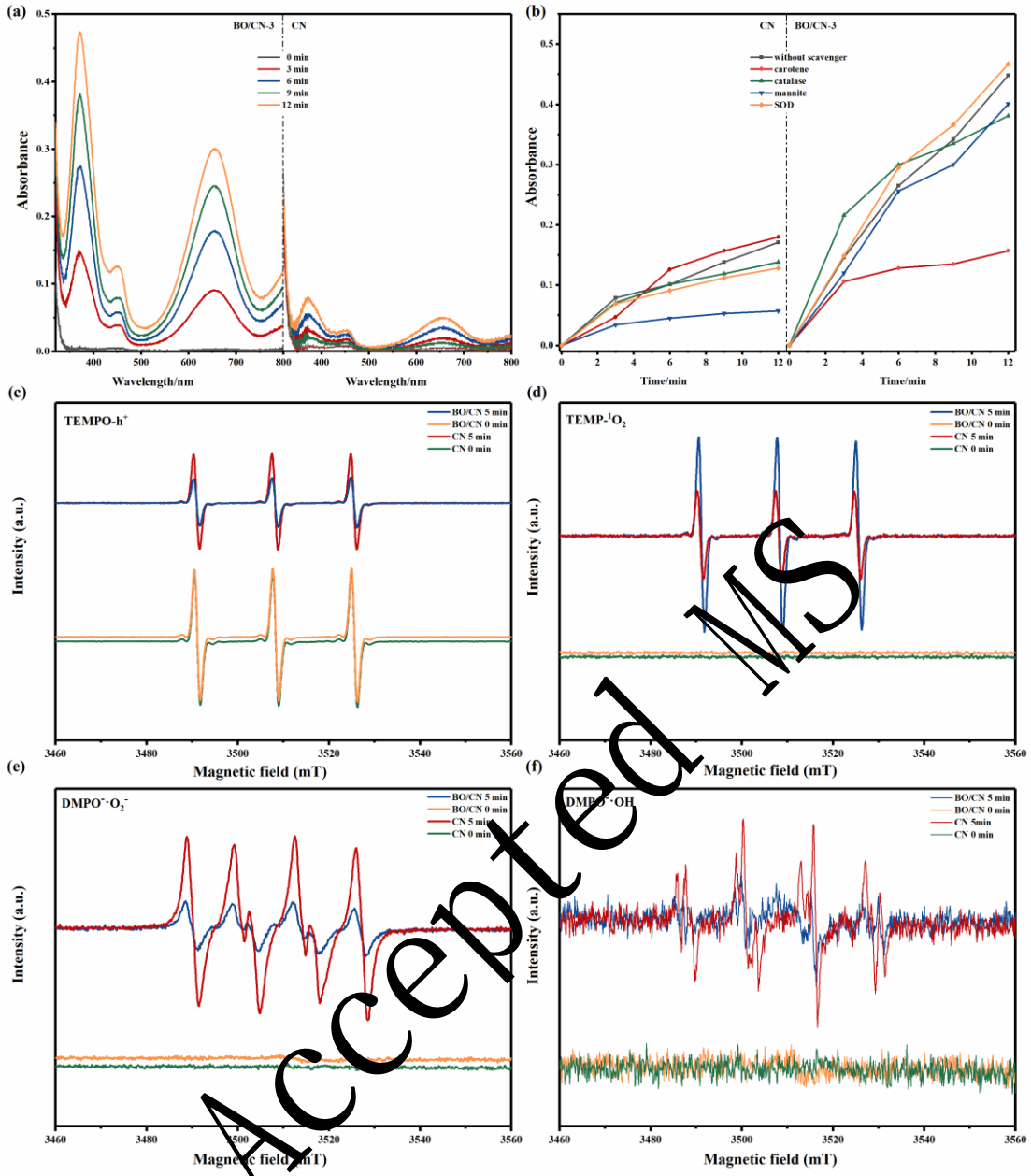

Figure. 10 (a) Time-dependent absorption spectra of TMB oxidation in air. (b) The absorbance of TMB oxidation with g-C_3N_4 and $Bi_2O_2CO_3$/g-C_3N_4 composites monitored at 380 nm in the presence of different scavengers. EPR spectra of radical adducts trapped by TEMPO (h^+), TEMP ($^1O_2$) and DMPO ($\bullet O_2^-$ and •OH) in different sample dispersion in the dark and under visible-light irradiation: (c) in aqueous dispersion for TEMPO- h^+, (d) in aqueous dispersion for TEMP-$^1O_2$, (e) in aqueous dispersion for DMPO -$\bullet O_2^-$, (f) in methanol dispersion for DMPO-•OH.

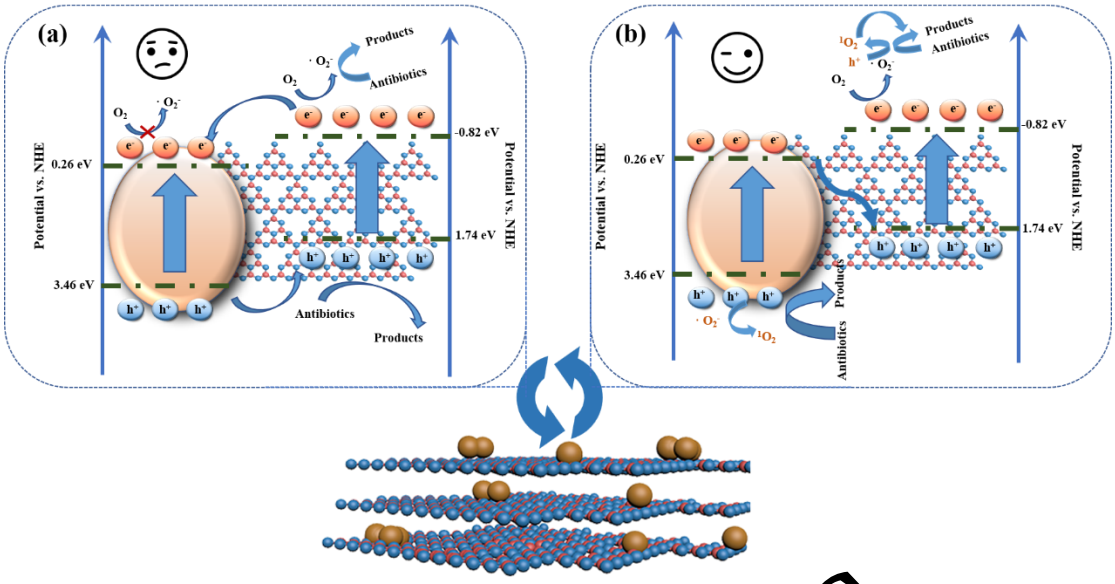

827

828 **Scheme 2.** Possible mechanism for pollutant degradation and electron flow by BO/CN.

829